



Optical and photovoltaic properties of organic solar cells versus bulk-heterojunction morphologyNurzhan Asanov *Department of Physics, Nazarbayev University, Astana KZ-01000, Kazakhstan*Nora Schopp *First Solar, Inc., Perrysburg, Ohio 43551, USA*Constantinos Valagiannopoulos **School of Electrical and Computer Engineering, National Technical University of Athens, Athens GR-15780, Greece*Viktor Brus †*First Solar, Inc., Perrysburg, Ohio 43551, USA
and Department of Physics, Nazarbayev University, Astana KZ-01000, Kazakhstan* (Received 27 November 2023; revised 25 March 2024; accepted 26 March 2024; published 2 May 2024)

It has long been argued that the performance of organic bulk-heterojunction solar cells critically depends on the morphology of the active layer, a mixture of donor and acceptor materials in which the charge generation from sunlight occurs. In this work, optical homogenization principles are utilized to model the structure of the common active layer PM6:Y6. By systematically modifying the size and shape of Y6 acceptor inclusions within the morphology, we explore how these changes influence the refractive index and extinction coefficient of the resulting effective medium. A synergy of transfer matrix optical simulations with the Hecht equation is used to evaluate the effect of the inclusions features on the external quantum efficiency spectrum. The reported findings can be particularly helpful in the fabrication of similar classes of organic solar cells by indicating which aspects of active layer mixture may undermine the expected performance of the photovoltaic cells.

DOI: [10.1103/PhysRevB.109.205201](https://doi.org/10.1103/PhysRevB.109.205201)**I. INTRODUCTION**

Organic solar cells (OSCs) have emerged as a promising and innovative technology due to their lightweight, flexible, and cost-effective nature [1]. Extensive efforts have been made to improve their performance, and now remarkable photoconversion efficiencies exceeding 19% have been achieved [2]. Central to such a high efficiency of OSCs is the active layer, the absorbing blend in which photoexcitation and charge generation occur. It is composed of carbon-based donor and acceptor materials, which can be deposited monolayer-by-monolayer or mixed before deposition to create a so-called bulk-heterojunction layer [3,4]. Due to the increased contact area between the two materials, reduced path excitons travel to the interface, and because of the simpleness of fabrication, state-of-the-art OSCs are mostly composed of bulk-heterojunction active layers [5,6].

It is believed that one way to further improve the efficiency of OSCs is to controllably optimize the morphology of the active layer. Typically, researchers change the molecular design of the layer; the processing conditions, such as solvent additives or the posttreatment methods, such as thermal annealing [7]. These modifications, however, affect not only the mor-

phology of the layer but also other processes. For example, varying the donor:acceptor ratio results in different effective lifetimes of charge carriers [8], while the molecular weight of polymer donors influences the coherence length of the morphology as well as bulk and surface trap concentrations [9]. Different solvent additives, along with changing phase separation of the donor and acceptor materials, yield distinct electron and hole mobilities of the devices [10], whereas different thermal annealing temperatures affect not only the mobilities but also the built-in voltage [11]. Since the structure of the bulk-heterojunction active layer is disordered, it is challenging to experimentally evaluate its influence on different characteristics [12]. This calls for an equivalent mathematical model, the only available tool to unravel how sensitive the optical properties of the bulk-heterojunction active layer are to its morphology, with other parameters being fixed.

Given the fact that the active layer consists of two dispersive media, one way to mathematically model it is to employ optical homogenization principles. From Maxwell-Garnett mixing formulas and Bruggeman's effective medium approximations to Floquet-Bloch theory for spatially periodic systems, homogenization techniques have a long and evolving history of describing complex structures in simple ways [13,14]. Importantly, these approximations can capture the directional preference of electromagnetic media by taking into account the size and the boundary shape of the considered mixtures [15,16]. Usually, one component of the structure

*valagiannopoulos@ece.ntua.gr

†viktor.brus@firstsolar.com

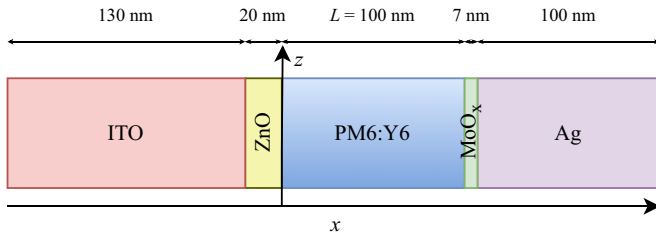


FIG. 1. Device structure of the organic solar cell studied in this work.

is referred to as a “host,” and the other is referred to as an “inclusion” while homogenization techniques yield their effective properties. By choosing models of the inclusions, we can organize the disordered nature of the active layer to further investigate how its morphology affects the optical and photovoltaic properties of the device.

In this work, we mathematically model the bulk-heterojunction morphology of a state-of-the-art active layer donor:acceptor blend, controllably modify the size or shape of the acceptor inclusions, and determine how these changes modulate the refractive index and extinction coefficient of the resultant effective medium. These optical properties are further used in transfer matrix optical simulations of OSCs for determining how the organic active layer bulk morphology exclusively affects the photovoltaic characteristics while keeping charge transport and recombination parameters invariant.

II. SYSTEM DESCRIPTION

A. Device structure and bulk-heterojunction texture

In Fig. 1, we depict a bulk-heterojunction organic solar cell comprising several layers stacked along the x axis with respect to the defined Cartesian coordinate system (x, y, z) . The structure is excited by a plane wave impinging normally at the leftmost surface and propagating across the $+x$ axis. The most important component of the considered device is the active layer, with a thickness equal to $L = 100$ nm. Therein, electric current is generated from sunlight; indeed, electrons and holes are produced due to the exchange of energy with the penetrating photons. The electrons are attracted by a thin (20 nm) ZnO layer due to the built-in potential difference, and then they are channeled to an indium tin oxide cathode (130 nm thick), where they are collected. Similarly, the developed holes travel to a silver anode (100 nm thick) after passing through a low work function molybdenum oxide film (7 nm thick).

Since we assume that the plane wave propagates along the x axis and meets the structure normally, the electric field vector will necessarily lie in the yz plane. As long as all functional materials of the considered device structure are isotropic, the orientation of the electric field vector plays no role. However, if any of the layers is filled with just a uniaxially anisotropic medium, characterized by relative permittivities along its major optical axes ϵ_z (z axis) and ϵ_{xy} (y axis), two problems have to be solved. In the first one, we consider the electric field vector parallel to the z axis and derive the function $E_z(x)$; in

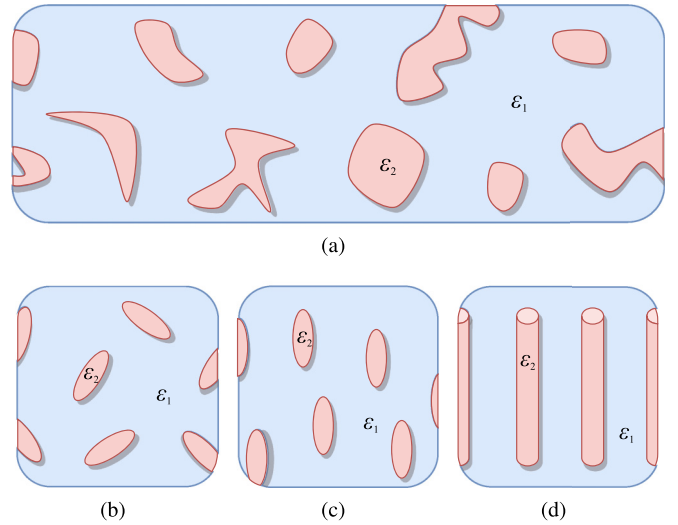


FIG. 2. (a) Example morphology of the active layer and its mathematical model with inclusions shaped as (b) random spheroids, (c) aligned spheroids, and (d) aligned cylinders.

the second one, it is parallel to the y axis, resulting in a field distribution $E_y(x)$. Any other orientation of the electric field vector can be treated as a linear combination of the respective solutions $E_z(x)$ and $E_y(x)$.

Given the fact that sunlight contains incoherent unpolarized light with all possible transverse directions of the electric field in its far region, we can find quantities related to the produced intensities by performing a weighted average of the respective quantities referring to the two orthogonal polarizations [17]. Therefore, all the macroscopic photovoltaic metrics can be obtained by taking into account 50% of the corresponding ones when electric field vector is assumed to be parallel to the z axis [$E_z(x)$] and 50% of the results regarding nonzero $E_y(x)$.

B. Active layer

The active layer of organic bulk-heterojunction solar cells is a combination of donor (PM6) and acceptor (Y6) materials, which are mixed chaotically, as shown in Fig. 2(a). Thus, it is difficult to identify the morphology effect on the electromagnetic and photovoltaic properties of the device. Consequently, we consider different scenarios regarding the size and shape of acceptor inclusions (relative permittivity ϵ_2) in the donor background matrix (relative permittivity ϵ_1).

The first scenario concerns identical ellipsoid particles of random orientation and location in the host, yielding an isotropic homogenized substance. The respective configuration is depicted in Fig. 2(b). In the second scenario in Fig. 2(c), the inclusions again have the same spheroidal shape but this time are aligned along the z axis, giving a directional preference to the mixture. The third scenario, as shown in Fig. 2(d), assumes lengthly cylindrical inclusions parallel to the z axis canonically placed in a rectangular grid.

To extract the effective homogenized quantities characterizing our blend, we need to know the dispersive electromagnetic responses for both of the ingredients, PM6 and Y6, whose chemical structures are depicted in Figs. 3(a)

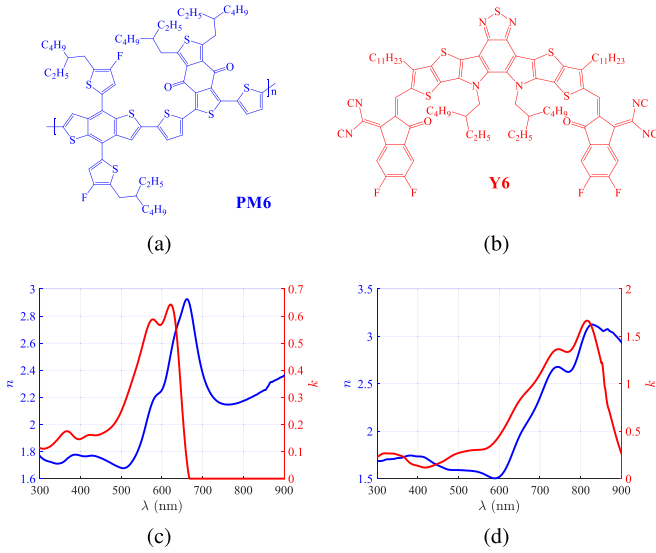


FIG. 3. (a) and (b) Chemical structure and (c) and (d) refractive index n and extinction coefficient k as a function of wavelength λ of donor PM6 and acceptor Y6 materials, respectively.

and 3(b), respectively. In Fig. 3(c), we represent the refractive index $n = n(\lambda)$ and the extinction coefficient $k = k(\lambda)$ of PM6 as functions of wavelength λ . They are calculated from reflectance $\rho = \rho(\lambda)$ and transmittance $\tau = \tau(\lambda)$ through a sample of length $L = 100$ nm, measured by a UV-visible-near-infrared (UV-VIS-NIR) Spectrometer (Lambda 1050, PerkinElmer Ltd.), as follows:

$$n = \frac{1 + \sqrt{\rho}}{1 - \sqrt{\rho}},$$

$$k = \frac{\lambda}{4\pi L} \ln \left[\frac{(1 - \rho)^2}{2\tau} + \sqrt{\frac{(1 - \rho)^4}{4\tau^2} + \rho^2} \right].$$

We notice that the extinction coefficient vanishes across the infrared band, while the refractive index maximizes when $k(\lambda)$ drops very abruptly, as dictated by Kramers-Kronig relations [18]. In Fig. 3(d), we show our measurement results for Y6 and notice that it is lossy across the entire investigated wavelength spectrum.

In the following, where mixture formulas are introduced, we mainly deal with complex relative permittivities ε , which are obtained from the measured refractive indexes n and extinction coefficients k as follows:

$$\varepsilon = (n - ik)^2.$$

C. Optical mixing principles

When inclusions are ellipsoid in shape, we assume that they are obtained from an ellipse with semiaxes (a, b) by rotation around its major axis, which is parallel to the z direction of our coordinate system. Therefore, we have axially symmetric particles of height $2b$ and equatorial radius a in their middle, characterized by the square eccentricity [13]:

$$e^2 = 1 - \left(\frac{a}{b}\right)^2. \quad (1)$$

This quantity can be either positive ($a < b$, giving $0 < e^2 < 1$), defining a prolate spheroid, or negative ($a > b$), corresponding to an oblate spheroid. Importantly, for $e^2 \rightarrow 1$ we obtain a flat circular disk normal to z axis, while a shape with $e^2 \rightarrow -\infty$ resembles a needle parallel to the z axis. On the other hand, obviously, a vanishing eccentricity, $e^2 = 0$, gives a sphere of radius $a = b$.

The way that each component of the electric field interacts with an ellipsoid particle is reflected in the different depolarization factors along each direction. In our axially symmetric case, we obtain $N_{xy} \equiv N_x = N_y$ and $N_z \neq N_{xy}$. In particular, for prolate spheroids, they are given by [13]

$$N_z = \frac{1 - e^2}{2e^3} \left(\ln \frac{1 + e}{1 - e} - 2e \right), \quad (2a)$$

$$N_{xy} = \frac{1 - N_z}{2}, \quad (2b)$$

while, for oblate spheroids, they are written as

$$N_z = \frac{e^2 - 1}{e^2} \left(1 - \frac{\arctan \sqrt{-e^2}}{\sqrt{-e^2}} \right), \quad (3a)$$

$$N_{xy} = \frac{1 - N_z}{2}. \quad (3b)$$

Different depolarization factors yield different effective relative permittivities $\varepsilon_x = \varepsilon_y = \varepsilon_{xy}$ and ε_z . When ellipsoid inclusions of the dielectric constant ε_2 have a random orientation and location in the host of the dielectric constant ε_1 , the blend can be considered isotropic, with effective permittivity given by [13]

$$\varepsilon_z = \varepsilon_{xy} = \varepsilon_1 + \varepsilon_1 \frac{\frac{f}{3} \sum_{j=x,y,z} \frac{\varepsilon_2 - \varepsilon_1}{\varepsilon_1 + N_j(\varepsilon_2 - \varepsilon_1)}}{1 - \frac{f}{3} \sum_{j=x,y,z} \frac{N_j(\varepsilon_2 - \varepsilon_1)}{\varepsilon_1 + N_j(\varepsilon_2 - \varepsilon_1)}}, \quad (4)$$

where f is the volume filling ratio of the particles in the background. The mixing law (4) originates from a combination of the Maxwell-Garnett theory [14] and the quasistatic solution of electromagnetic scattering by ellipsoids. In this way, the collective dynamics between various inclusions are extracted through the respective polarizability dyadics, followed by volume averaging. The depolarization factors N_j , with $j = x, y, z$, are computed via (2) for prolate spheroids and (3) for oblate spheroids. In the following, we will keep a constant $f = 0.5454$, which is commonly used in photovoltaic applications involving PM6:Y6 [19]. If the same ellipsoid inclusions are aligned along the z axis, giving the setup a directional preference, the isotropy will not hold, and two different homogenized dielectric constants (one along the z direction and one across the xy plane) emerge, as follows [13]:

$$\varepsilon_z = \varepsilon_1 + f\varepsilon_1 \frac{\varepsilon_2 - \varepsilon_1}{\varepsilon_1 + (1 - f)N_z(\varepsilon_2 - \varepsilon_1)}, \quad (5a)$$

$$\varepsilon_{xy} = \varepsilon_1 + f\varepsilon_1 \frac{\varepsilon_2 - \varepsilon_1}{\varepsilon_1 + (1 - f)N_{xy}(\varepsilon_2 - \varepsilon_1)}. \quad (5b)$$

Formulas (4) and (5) correspond to the case of an unbounded region and thus do not take into account the presence of interfaces, as shown in Fig. 1. However, they can be employed to model the light-matter interactions in our configuration since the size of inclusions is assumed to be much

smaller than the volume of the active layer. Indeed, along its length ($L = 100$ nm) may contain numerous ellipsoid inclusions, while its transverse dimensions are huge (20×15 mm²).

In the case of cylindrical inclusions [20] with radius a , we assume that they are placed in a rectangular grid with side $b > a$ and aligned along the z axis, yielding a volume filling ratio $f = \pi a^2 / (2b)^2$. Again, the blend will be anisotropic, with effective relative permittivities written as [17]

$$\varepsilon_z = \varepsilon_1 \left[1 + f \frac{(2\varepsilon_2/\varepsilon_1 - 1)g(k_0 a \sqrt{\varepsilon_2}) - 1}{g(k_0 a \sqrt{\varepsilon_2}) + 1} \right], \quad (6a)$$

$$\varepsilon_{xy} = \varepsilon_1 \left[1 + 2f \frac{(\varepsilon_2/\varepsilon_1)g(k_0 a \sqrt{\varepsilon_2}) - 1}{(\varepsilon_2/\varepsilon_1)g(k_0 a \sqrt{\varepsilon_2}) + 1} \right]. \quad (6b)$$

The symbol $k_0 = 2\pi/\lambda$ is used for the free-space wave number, the function $g(x)$ is defined as $g(x) = \frac{J_m(x)}{xJ_0(x) - J_1(x)}$, and J_m denotes the m -th order Bessel function. The adopted model uses the polarization currents associated with the supported Bloch modes across the lattice, which are expressed via the various dipole and quadrupole moments [21]. Importantly, the homogenized formulas (6) are more complicated than the respective ones for spheroid inclusions (4) and (5) since they describe the dynamics of multiple dipolar interactions and contain transcendental functions. Such complexity grants the model versatility and renders it valid, even if the constraint $L \gg a$ is not thoroughly respected.

D. Photovoltaic properties

Given the refractive index $n(\lambda)$ and extinction coefficient $k(\lambda)$ of all layers of the organic solar cell depicted in Fig. 1, its photovoltaic description is based on calculations implementing the so-called transfer-matrix method [22–24] combined with the multimechanism recombination model and Hecht equation [8,25]. This technique calculates the electric field $E(x)$ in the active layer of the device, which is related to the free charge carrier generation rate $G(x, \lambda)$ via

$$G(x, \lambda) = 2\pi \frac{\varepsilon_0}{h} n(\lambda) k(\lambda) |E(x)|^2, \quad (7)$$

where h is the Plank constant and ε_0 is the permittivity in vacuum. If one accounts for all generation rates characterizing the entire operational wavelength range $\lambda_{\min} < \lambda < \lambda_{\max}$, with $\lambda_{\min} = 300$ nm and $\lambda_{\max} = 900$ nm, one obtains the integral

$$G'(x) = \int_{\lambda_{\min}}^{\lambda_{\max}} G(x, \lambda) d\lambda. \quad (8)$$

This quantity is called the spatial generation rate.

Importantly, (7) assumes that photons create electrons and holes 100% of the time; however, the photoexcited electron-hole pair might not split into free charge carriers. Instead, they might recombine immediately after excitation, a process called geminate recombination. The complementary probability of this effect is called the geminate prefactor, denoted by P_g , and indicates how many photons will generate free charge carriers.

Upon generation, the free electrons and holes drift towards the respective electrodes, creating current. However, as they move, different charge carriers might meet each other and recombine, a process called nongeminate recombination. This

can happen when the electrons and holes recombine either through trap states in the bulk (bulk trap-assisted recombination) or on the surface (surface trap-assisted recombination) of the active layer electrode interface. In addition, recombination occurs when the electrons and holes recombine from band to band (bimolecular recombination).

The aforementioned nongeminate recombination processes are expressed through the mean free path w that the charge carriers travel to the active layer before getting recombined [25]. In the considered simulations, regardless of the type, size, or orientation of inclusions, we found [8] the length of the path within the narrow range $60 < w < 64$ nm. In our theoretical model, we consider $L = 100$ nm and thus $L > w$; as a result, the efficiency evaluated via our simulations is expected to be lower than that of similar experimental setups in which w is much more substantial [26,27]. On this front, one should also note that all possible mechanisms of recombination losses (bimolecular, bulk, and surface trap-assisted recombination) are taken into account in our theoretical study to represent the most general case of the example of PM6:Y6 material properties. Obviously, the bigger w gets, the greater the number of electrons and holes that reach the respective electrodes before recombining gets. Therefore, we model our device under short-circuit conditions; we account only for the corresponding charge carriers [25]. Electrons that are generated at position x are closer to the positive electrode ($x = 0$) the smaller x gets and thus have increased probability to reach it and create the desired current in the active layer. This probability is denoted by $\eta_n(x)$ and should be a decreasing function of x . Similarly, a hole generated at a position x will travel along the positive axis towards the negative electrode at $x = L$ and has a probability of arriving equal to $\eta_p(x)$, increasing with x [28]. Since the two events are disjoint, the probability of having current $\eta(x)$ will just be the sum of the two probabilities, which is given by the Hecht equation [29]:

$$\eta(x) \equiv \eta_n(x) + \eta_p(x) = \frac{w}{L} \left[1 - \exp\left(\frac{x-L}{w}\right) \right] + \frac{w}{L} \left[1 - \exp\left(-\frac{x}{w}\right) \right]. \quad (9)$$

Considering all the recombination processes, the quantity $P_g G(x, \lambda) \eta(x)$ expresses the actual number of electrons and holes per unit volume per time per unit wavelength that will reach the electrodes and create a current. Integration of this quantity from (9) over the active layer depth x and multiplication by the elementary charge q will give us the short-circuit current density $J_{sc}(\lambda)$ [25]:

$$J_{sc}(\lambda) = q P_g \int_0^L G(x, \lambda) \eta(x) dx. \quad (10)$$

Such a quantity equals the current density at zero voltage, and the higher it is, the more effectively our device operates.

External quantum efficiency $\text{EQE}(\lambda)$ can be calculated from (10) and equals the ratio of the generated flux of charge carriers to the incident flux of photons with given energy [25]:

$$\text{EQE}(\lambda) = \frac{J_{sc}(\lambda)}{q} \frac{h\nu}{I_0(\lambda)}, \quad (11)$$

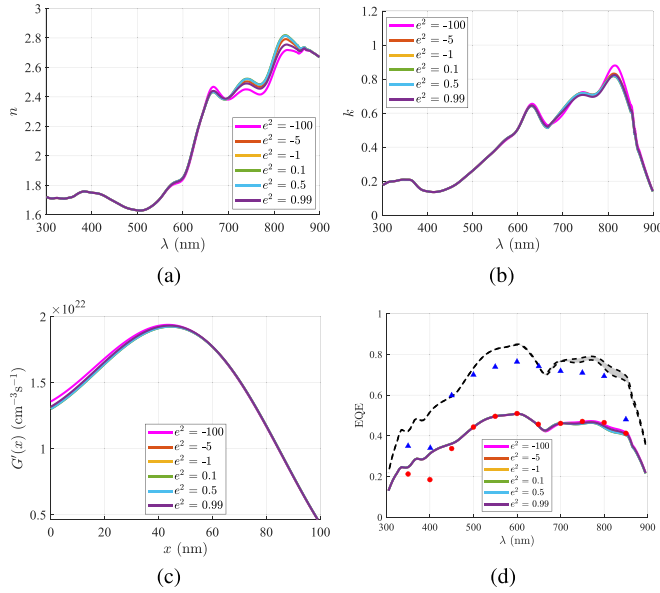


FIG. 4. Randomly oriented spheroid inclusions of varying square eccentricity e^2 : (a) Modeled refractive index $n(\lambda)$ and (b) extinction coefficient $k(\lambda)$ of the PM6:Y6 blend. (c) Spatially dependent generation rate $G'(x)$ and (d) EQE of the device in the actual and ideal cases, accompanied by two sets of measurements [31] of different molecular orientations of the same PM6:Y6 mixture.

where ν is the frequency of incoming photons and $I_0(\lambda)$ is the solar power distribution as a function of the operational wavelength λ .

III. NUMERICAL RESULTS

A. Random spheroid inclusions

In Figs. 4(a) and 4(b), we present the refractive index n and the extinction coefficient k as a function of wavelength λ for the first scenario. In particular, we assume that the active layer consists of randomly oriented spheroid acceptor inclusions in the donor matrix, as shown in Fig. 2(b). The alternative configuration, namely, donor inclusions in the acceptor matrix while keeping the same volume portion for each material, was examined and found to yield similar results, mostly because the volume filling ratio f is selected to be close to 0.5; the respective variations are not shown for brevity. Since the blend is isotropic, the electric field vector will interact with the homogenized $\epsilon_{xy} = \epsilon_z$ of the active layer as given by (4). We can see that, on average, $n(\lambda)$ is an increasing function of λ , regardless of the shape of the spheroid; similarly, $k(\lambda)$ also increases, but beyond infrared $\lambda \cong 810$ nm, it drops dramatically. We also observe that different e^2 yield insignificant differences in the values of $n(\lambda)$ and $k(\lambda)$ and that this variation is even smaller for the $G'(x)$ and EQE values. It is remarkable that the experimental measurements of the complex refractive index for an actual PM6:Y6 sample [30] with the same filling factor ($f = 0.5454$) are in good agreement with the effective-medium-based theoretical results in Figs. 4(a) and 4(b). By inspecting Fig. 4(c), we understand that the spatial generation rate $G'(x)$ from (8) is maximized internally to the active layer, which means that most excitons

are generated therein. Moreover, the shape of $G'(x)$ resembles a standing wave pattern with a peak shifted from the middle of the active layer. That is because of the unequal magnitudes of the two oppositely propagating waves comprising the electric field. As far as the EQE wavelength dispersion from (11) is concerned [Fig. 4(d)], its maximum appears at $\lambda \cong 600$ nm, within the visible spectrum. We also show a gray zone, every single point of which corresponds to an ideal case with $P_g = 1$ and $\eta(x) = 1$, that is, assumes that all photons will generate free charges and all carriers close the circuit to create current. We do not show one curve since we implicitly sweep the parameter e^2 to observe the extreme values of EQE. Obviously, that second set of data, labeled the “ideal scenario,” yields to more substantial EQE compared to the respective scores for the considered realistic case.

On top of these two sets of data, we depict the results of two experimental measurements. They are taken from [31] and correspond to two different molecular orientations controlled by choosing solvents with different boiling points, such as chloroform (blue triangles) and chlorobenzene (red dots). By using them, we demonstrate the huge influence of donor-acceptor topology on the performance of our solar cell, even though the PM6:Y6 blend used is identical. Therefore, we argue that the goal of our model is not to simulate experimental results, which is not possible without prior knowledge of the exact configuration of the measured active layer. On the contrary, we assume that we have sufficient information regarding the volume distribution occupied by the two media (PM6, Y6), and we evaluate the photovoltaic response scores of the considered organic solar cells. In this research framework, we regard different morphologies (random spheroid, aligned spheroid, and cylindrical Y6 particles) and wave polarizations to compute the setup’s performance based on the respective homogenization principles and effective medium formulas.

B. Aligned spheroid inclusions

When it comes to the case of spheroid inclusions aligned along the z axis [Fig. 2(c)], the device will operate differently in relation to the direction of the electric field E . In Fig. 5, we assume that the vector of the electric field is parallel to the z axis; thus, it will interact only with the ϵ_z component of the homogenized active layer given by (5a). In Figs. 5(a) and 5(b), we depict the refractive index $n(\lambda)$ and extinction coefficient $k(\lambda)$ along the z axis. Unlike the case of randomly oriented particles, we observe that the inclusion shape affects the values of $n(\lambda)$ and $k(\lambda)$ across the red part of the spectrum. More specifically, $n(\lambda)$ decreases with e^2 , while $k(\lambda)$, on average, demonstrates the opposite trend. Regarding the spatial generation rate $G'(x)$ [Fig. 5(c)], the square eccentricity plays a role for observation points close to the front surface of the active layer. In Fig. 5(d), we show the curves EQE(λ) for several e^2 and observe that the more oblate the spheroids are, the higher the recorded efficiencies get in the red spectrum. It should be noted that the performance evaluation (EQE) of our photovoltaic cells is not based only on the optical properties of the active layer; indeed, for $\lambda < 300$ nm, EQE vanishes since the ITO layer does not transmit light. As in Fig. 4(d), we also represent the respective ideal scenario and obtain another gray zone whose range indicates the effect of the implicit parameter

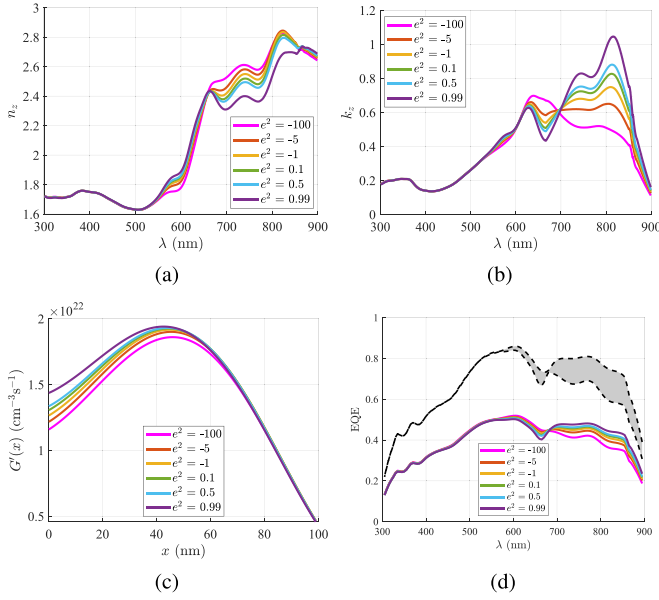


FIG. 5. Aligned spheroid inclusions of varying square eccentricity e^2 with the electric field vector along the z axis: (a) Modeled refractive index $n(\lambda)$ and (b) extinction coefficient $k(\lambda)$ of the PM6:Y6 blend. (c) Spatially dependent generation rate $G'(x)$ and (d) EQE of the device in the actual and ideal cases.

e^2 on EQE, it is similar to that of the original bunch of curves. Once again, the score for an ideal setup [$P_g = 1$ and $\eta(x) = 1$] is higher than those for the cases in which several sorts of losses are taken into account; such a conclusion is valid at every single operational wavelength λ in the visible range. However, the reported results cannot be used to reproduce the experimental data where the PM6:Y6 topology is not well known.

In Fig. 6, we assume that the electric field vector is parallel to the y axis; thus, it will interact with the permittivity ϵ_{xy} of the same structure, given by (5b). Since the electric field direction is normal to the direction considered in Fig. 5, the dependence of all of the represented quantities on e^2 will be the opposite. Indeed, e^2 determines the distribution of the particle around the z axis, and thus, the spatial generation rate $G'(x)$ will benefit from more prolate spheroids. The same trend is observed for the EQE, especially under red color illumination and near infrared.

C. Aligned cylindrical inclusions

The last scenario, depicted in Fig. 2(d), concerns the case of cylinder inclusions aligned along the z axis. Just like in the case of aligned spheroid inclusions, the structure is anisotropic, and its properties depend on the direction of the electric field. In Fig. 7, we assume that the electric field vector is parallel to the z axis, interacting only with ϵ_z of the homogenized blend expressed by (6a). In Figs. 7(a) and 7(b), we illustrate the refractive index $n(\lambda)$ and extinction coefficient $k(\lambda)$ of the blend along the z axis for various cylinder radii a . In Sec. III B, the shape of inclusions affected the refractive index for red and near-infrared wavelengths λ ; nonetheless, in Sec. III C, $n(\lambda)$ is mostly dependent on the size of inclusions in the ultraviolet and violet wavelengths. The extinction

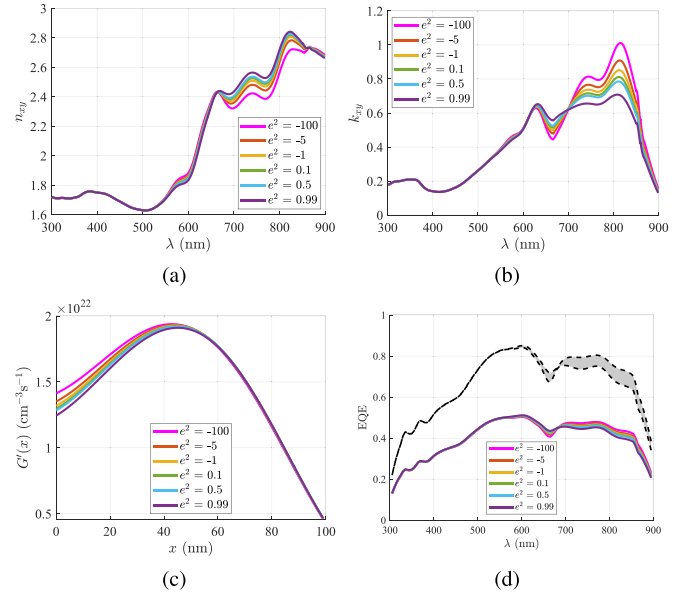


FIG. 6. Aligned spheroid inclusions of varying square eccentricity e^2 with the electric field vector along the y axis: (a) Modeled refractive index $n(\lambda)$ and (b) extinction coefficient $k(\lambda)$ of the PM6:Y6 blend. (c) Spatially dependent generation rate $G'(x)$ and (d) EQE of the device in the actual and ideal cases.

coefficient $k(\lambda)$, on the other hand, is slightly affected by the radius a in the ultraviolet and mainly in the red spectrum. In Fig. 7(c), we depict the variation of the spatial generation rate $G'(x)$ and can see that the radius of the inclusions has a slight effect on the front surface of the active layer. As far as the EQE is concerned, in both the ideal and actual scenarios, the size of the inclusions plays a tiny role in the ultraviolet part of the spectrum, as observed in Fig. 7(d). The performance

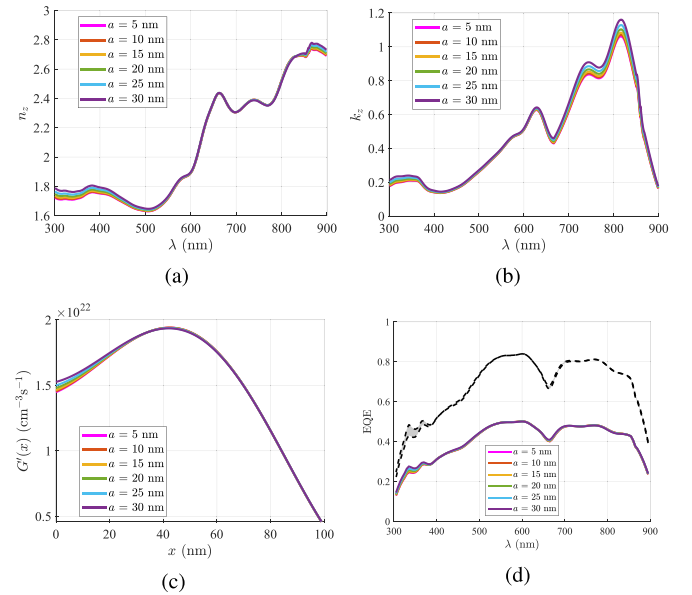


FIG. 7. Aligned cylinder inclusions of varying radius a with the electric field vector along the z axis: (a) Modeled refractive index $n(\lambda)$ and (b) extinction coefficient $k(\lambda)$ of the PM6:Y6 blend. (c) Spatially dependent generation rate $G'(x)$ and (d) EQE of the device in the actual and ideal cases.

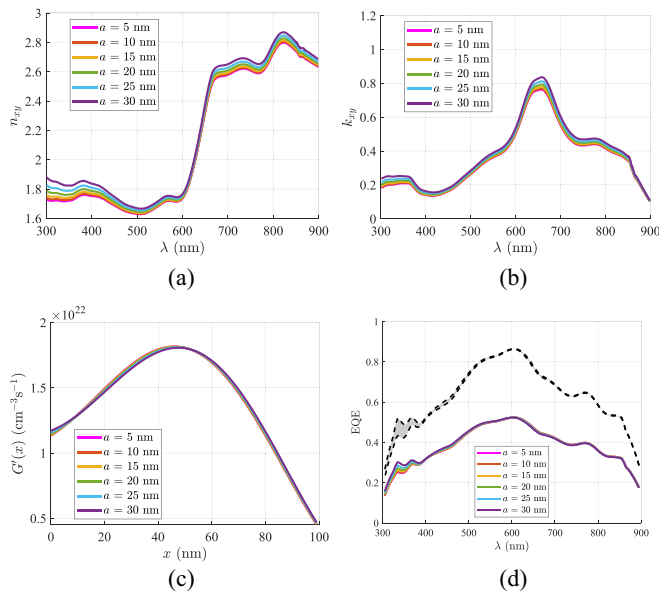


FIG. 8. Aligned cylinder inclusions of varying radius a with the electric field vector along the y axis: (a) Modeled refractive index $n(\lambda)$ and (b) extinction coefficient $k(\lambda)$ of the PM6:Y6 blend. (c) Spatially dependent generation rate $G'(x)$ and (d) EQE of the device in the actual and ideal cases.

graphs are qualitatively in agreement with what is obtained from real-world configurations [26]. Indeed, all sets of data give squared curved shapes with a maximum at $\lambda \cong 600$ nm; in addition, for $\lambda > 900$ nm, EQE tends to zero due to the emerging band gap of the utilized PM6:Y6 active layer [19]. However, by no means can we use the described theoretical homogenization model to reproduce quantitatively the experimental measurements since they are strongly connected to the topology of the donor and acceptor in the active layer [31].

In Fig. 8, we assume an electric field vector that is parallel to the y axis, which will again interact with the permittivity ϵ_{xy} of the structure, given by (6b). The radius of the cylinders a influences the refractive index $n(\lambda)$ across the entire investigated spectrum [Fig. 8(a)]; in particular, the larger the cylinders are, the higher the refractive index of the homogenized active layer is. From Fig. 8(b), we observe the same trend for the extinction coefficient $k(\lambda)$. Interestingly, the maximum loss shifts from the infrared region to the orange region. As depicted in Fig. 8(c), the spatial generation rate $G'(x)$ along the xy plane

is not affected by the radius of the inclusions at all. When it comes to EQE in both the actual and ideal cases, as shown in Fig. 8(d), it changes only mildly with a exclusively in the ultraviolet region.

IV. CONCLUSION

Using the optical mixing principles, the active layer of state-of-the-art organic bulk-heterojunction solar cells was modeled by incorporating acceptor inclusions of varying sizes, shapes, and orientations in the donor material. Our analysis revealed that changes in size cause little difference in the optical and photovoltaic properties of the device, while distinct shapes yield significant variations, especially in the red spectrum of visible light. When aligned, the more oblate spheroid inclusions result in a blend with higher absorption. That effect gives rise to more excitons being generated and a higher external quantum efficiency in the red-colored frequency band, if the electric field is polarized along the axis of the particles. On the contrary, if the electric field is normal to their axis, the opposite trend is observed: more prolate spheroid inclusions yield improved absorbance of the layer and lead to levels of enhanced efficiency.

The reported findings give a mathematical validation of the long-standing belief that the active layer morphology indeed plays a critical role in the photovoltaic properties of organic solar cells. Therefore, the optical mixing techniques could become a powerful tool to further explore the intricate relationship between the morphologies of different bulk-heterojunction layers and the efficacy of the solar cells. Importantly, this approach can be used to predict solar cell behavior based on the donor and acceptor materials and their optical properties. As a result, the process followed here could guide and accelerate organic photovoltaic inverse design and development.

ACKNOWLEDGMENTS

This work received funding from Nazarbayev University, Kazakhstan, under the Collaborative Research Grant Project “Waves Interaction with CARbon Nanotubes - WICAN,” Grant Award No. 20122022CRP1607. This work is supported by the Collaborative Research Program Grant of Nazarbayev University Grant No. 11022021CRP1505 and the Faculty-Development Competitive Research Program Grant of Nazarbayev University Grant No. 11022021FD2915.

- [1] M. Riede, D. Spoltore, and K. Leo, Organic solar cells - The path to commercial success, *Adv. Energy Mater.* **11**, 2002653 (2021).
- [2] L. Zhu *et al.*, Single-junction organic solar cells with over 19% efficiency enabled by a refined double-fibril network morphology, *Nat. Mater.* **21**, 656 (2022).
- [3] R. Sun *et al.*, A universal layer-by-layer solution-processing approach for efficient non-fullerene organic solar cells, *Energy Environ. Sci.* **12**, 384 (2019).
- [4] A. Wadsworth, Z. Hamid, J. Kosco, N. Gasparini, and I. McCulloch, The bulk heterojunction in organic photovoltaic,

photodetector, and photocatalytic applications, *Adv. Mater.* **32**, 2001763 (2020).

- [5] A. Uddin, Organic solar cells, *Comprehensive Guide on Organic and Inorganic Solar Cells* (Elsevier, Chennai, India, 2022), pp. 25–55.
- [6] G. Perrakis, A. C. Tasolamprou, G. Kenanakis, E. N. Economou, S. Tzortzakakis, and M. Kafesaki, Combined nano and micro structuring for enhanced radiative cooling and efficiency of photovoltaic cells, *Sci. Rep.* **11**, 11552 (2021).
- [7] F. Zhao, C. Wang, and X. Zhan, Morphology control in organic solar cells, *Adv. Energy Mater.* **8**, 1703147 (2018).

- [8] N. Schopp, G. Akhtanova, P. Panoy, A. Arbuz, S. Chae, A. Yi, H. J. Kim, V. Promarak, T.-Q. Nguyen, and V. V. Brus, Unraveling device physics of dilute-donor narrow-bandgap organic solar cells with highly transparent active layers, *Adv. Mater.* **34**, 2203796 (2022).
- [9] N. Schopp *et al.*, Organic photovoltaic performance resiliency: Role of molecular weight in a PM7 derivative, *ACS Energy Letters* **8**, 3307 (2023).
- [10] C. McDowell, M. Abdelsamie, M. F. Toney, and G. C. Bazan, Solvent additives: Key morphology-directing agents for solution-processed organic solar cells, *Adv. Mater.* **30**, 1707114 (2018).
- [11] M. B. Upama, N. K. Elumalai, M. A. Mahmud, M. Wright, D. Wang, C. Xu, and A. Uddin, Effect of annealing dependent blend morphology and dielectric properties on the performance and stability of non-fullerene organic solar cells, *Sol. Energy Mater. Sol. Cells* **176**, 109 (2018).
- [12] N. Mohammadi Estakhri, C. Argyropoulos, and A. Alù, Graded metascreens to enable a new degree of nanoscale light management, *Philos. Trans. R. Soc. A* **373**, 20140351 (2015).
- [13] A. Sihvola, *Electromagnetic Mixing Formulas and Applications* (Institution of Electrical Engineers, London, 1999).
- [14] A. Sihvola, Homogenization principles and effect of mixing on dielectric behavior, *Photonics Nanostruct.* **11**, 364 (2013).
- [15] C. A. Valagiannopoulos, On examining the influence of a thin dielectric strip posed across the diameter of a penetrable radiating cylinder, *Prog. Electromagn. Res. C* **3**, 203 (2008).
- [16] C. A. Valagiannopoulos, Study of an electrically anisotropic cylinder excited magnetically by a straight strip line, *Prog. Electromagn. Res.* **73**, 297 (2007).
- [17] C. A. Valagiannopoulos and P. G. Lagoudakis, Photonic crystals for optimal color conversion in light-emitting diodes: A semi-analytical approach, *J. Opt. Soc. Am. B* **35**, 1105 (2018).
- [18] S. Horsley, M. Artoni, and G. La Rocca, Spatial Kramers-Kronig relations and the reflection of waves, *Nat. Photonics* **9**, 436 (2015).
- [19] J. Yuan, Y. Zhang, L. Zhou, G. Zhang, H.-L. Yip, T.-K. Lau, X. Lu, C. Zhu, H. Peng, P. A. Johnson, M. Leclerc, Y. Cao, J. Ulanski, Y. Li, and Y. Zou, Single-junction organic solar cell with over 15% efficiency using fused-ring acceptor with electron-deficient core, *Joule* **3**, 1140 (2019).
- [20] K. Mahmood, B. S. Swain, A. R. Kirmani, and A. Amassian, Highly efficient perovskite solar cells based on a nanostructured WO₃-TiO₂ core-shell electron transporting material, *J. Mater. Chem. A* **3**, 9051 (2015).
- [21] I. Chremmos, E. Kallos, M. Giamalaki, V. Yannopapas and E. Paspalakis, Effective medium theory for two-dimensional non-magnetic metamaterial lattices up to quadrupole expansions, *J. Opt.* **17**, 075102 (2015).
- [22] M. N. Polyanskiy, Refractive index database, <https://refractiveindex.info>.
- [23] G. F. Burkhard, E. T. Hoke, and M. D. McGehee, Accounting for interference, scattering, and electrode absorption to make accurate internal quantum efficiency measurements in organic and other thin solar cells, *Adv. Mater.* **22**, 3293 (2010).
- [24] N. Schopp, V. V. Brus, J. Lee, G. C. Bazan, and T.-Q. Nguyen, A simple approach for unraveling optoelectronic processes in organic solar cells under short-circuit conditions, *Adv. Energy Mater.* **11**, 2002760 (2021).
- [25] N. Schopp, V. V. Brus, and T.-Q. Nguyen, On optoelectronic processes in organic solar cells: From opaque to transparent, *Adv. Opt. Mater.* **9**, 2001484 (2021).
- [26] Y. Li *et al.*, Lifetime over 10000 hours for organic solar cells with Ir/IrOx electron-transporting layer, *Nat. Commun.* **14**, 1241 (2023).
- [27] S. Shoaee, H. M. Luong, J. Song, Y. Zou, T.-Q. Nguyen, and D. Neher, What we have learnt from PM6:Y6, *Adv. Mater.* **8**, 2302005 (2023).
- [28] J. C. Blakesley and D. Neher, Relationship between energetic disorder and open-circuit voltage in bulk heterojunction organic solar cells, *Phys. Rev. B* **84**, 075210 (2011).
- [29] K. Hecht, Zum Mechanismus des lichtelektrischen Primärstromes in isolierenden Kristallen, *Z. Angew. Phys.* **77**, 235 (1932).
- [30] R. Kerremans, C. Kaiser, W. Li, N. Zarrabi, P. Meredith, and A. Armin, The optical constants of solution-processed semiconductors-New challenges with perovskites and non-fullerene acceptors, *Adv. Opt. Mater.* **8**, 2000319 (2020).
- [31] Y. Fu *et al.*, Molecular orientation-dependent energetic shifts in solution-processed non-fullerene acceptors and their impact on organic photovoltaic performance, *Nat. Commun.* **14**, 1870 (2023).